INTERNATIONAL JOURNAL FOR NUMERICAL METHODS IN FLUIDS, VOL. 7, 197–213 (1987)

# A HODOGRAPH-BASED METHOD FOR THE DESIGN OF SHOCK-FREE CASCADES

A. A. HASSAN*

*Arizona State University, Tempe, Arizona 85287, U.S.A.*

AND

G. S. DULIKRAVICH†

*The Pennsylvania State University, University Park, PA 16802, U.S.A.*

## SUMMARY

A hodograph-based method, originally developed by the first author for the design of shock-free aerofoils, has been modified and extended to allow for the design of shock-free compressor blades. In the present procedure, the subsonic and supersonic regions of the flow are decoupled, allowing the solution of either an elliptic or a hyperbolic-type partial differential equation for the stream function. The coupling of both regions of the flow is carried out along the sonic line which adjoins both regions. For the subcritical portion of the flow considered here, the pressure distribution is prescribed in addition to the upstream and downstream flow conditions. For the supercritical portion of the flow, the stream function on the sonic line is given instead of the supercritical pressure distribution which is found as part of the solution. In the special hodograph variables used, the equation for the stream function is solved iteratively using a second-order accurate line relaxation procedure for the subsonic portion of the flow. For the supercritical portion of the flow, a characteristic marching procedure in the hodograph plane is used to solve for the supersonic flow. The results are then mapped back to the physical plane to determine the blade shape and the supercritical pressures. Examples of shock-free compressor blade designs are presented. They show good agreement with the direct computation of the flow past the designed blade.

KEYWORDS Transonic Hodograph Shock-free Cascades

## INTRODUCTION

The design of light and efficient turbomachinery components is currently receiving considerable attention in the aerodynamic community. The recent trends towards obtaining higher blade loading has driven the operating conditions of modern compressors and turbines into the transonic regime. Unfortunately, once local regions of the internal flow become supersonic, complex shock patterns are likely to occur with the attendant wave drag and shock-induced boundary-layer separation losses. Consequently, noise and vibration levels increase drastically and an overall rapid decline of the aerodynamic efficiency of the cascade is observed. A shock-free flow would, of course, be desirable, as it avoids these losses. In this special class of flows, the fluid decelerates from a supersonic Mach number to a subsonic Mach number smoothly over the surface of the blade. The unique geometry of the blade prevents the coalescence[1,2] of the

*Assistant Professor, Mechanical and Aerospace Engineering Department.
†Associate Professor, Department of Aerospace Engineering.

0271–2091/87/030197–17$08.50

*Received 5 May 1986*

reflected (of the sonic line) weak compression Mach waves which would otherwise lead to a finite terminal shock wave. Therefore, careful blade 'profiling' or shaping is required in this velocity range, especially for the decelerated compressor cascade flow.

Although major progress has been made in the analysis (direct problem) of transonic cascade flows,[3-6] only a limited number of global design (inverse problem) techniques, to date, have been developed for obtaining shock-free cascade flows. The method of complex characteristics developed by Garabedian[7,8] and later applied by Korn[9] for the design of shock-free blades is mathematically elegant. However, even in its user-orientated version, practical use of the method requires much experience and mathematical insight. Another indirect approach was developed by Sobieczky.[10,11] Here, the rheoelectric analogy to the compressible flow equations was used to define a number of shock-free cascades. This unique method has not yet found wide acceptance in practical blade design applications owing to its complex hardware requirements. An intermediate position between analysis and design (i.e. semi-inverse) is taken by the fictitious gas approach developed by Sobieczky.[12] This approach, first adopted by Dulikravich and Sobieczky,[13,14] and later by Beauchamp[15] and many others,[16-18] provides an inverse treatment only in the supersonic part of the blade contour. That is, while fixing the known subsonic boundary of the blade, the supersonic boundary is redesigned to eliminate any existing shock waves.

The design procedure developed here is an improvement of Sobieczky's rheoelectrical analogy method.[10,11] Since the use of an electrical setup, of course, did not provide for economical use of the method, it did lead to a greater understanding of this indirect approach. By replacing the electric analogue by a fast elliptic solver (Hassan[19] and Hassan *et al.*[20]), we could use all the experience of the analogue method concerning boundary conditions that result in interesting aerofoil and blade designs. The procedure requires less than two minutes of IBM 3081 CPU time for the design of a subcritical or a supercritical blade section. Though the method is limited to two-dimensional flow, it does allow the user to specify a desired pressure distribution and achieve it with little difficulty through an iterative process.

## MATHEMATICAL FORMULATION

We consider steady, two-dimensional, compressible, irrotational flow of a perfect gas. The governing equations of motion are

continuity
$$\nabla \cdot \rho \mathbf{q} = 0, \tag{1}$$

irrotationality
$$\nabla \times \mathbf{q} = 0, \tag{2}$$

and
$$\frac{p}{\rho^{\gamma}} = \text{constant}. \tag{3}$$

Equations (1) and (2) are identically satisfied by introducing the usual compressible stream function $\psi$ and the velocity potential $\phi$ defined through the following relations,

$$\begin{aligned} \rho u &= \psi_y = \phi_x, \\ \rho v &= -\psi_x = \phi_y. \end{aligned} \tag{4}$$

Through cross-differentiation, equations (4) can thus be reduced to a single equation in either $\phi$ or $\psi$, viz.,

$$\psi_{xx} + \psi_{yy} = \left(\frac{\rho_x}{\rho}\right)\psi_x + \left(\frac{\rho_y}{\rho}\right)\psi_y, \tag{5}$$

$$\phi_{xx} + \phi_{yy} = -\left(\frac{\rho_x}{\rho}\right)\phi_x - \left(\frac{\rho_y}{\rho}\right)\phi_y, \tag{6}$$

with

$$\rho = \rho(q), \quad q = |\nabla\phi|.$$

It can be easily shown that equations (5) and (6) are elliptic for $M < 1$ (subsonic flow), hyperbolic for $M > 1$ (supersonic flow), and parabolic where $M = 1$ (sonic flow). To solve either of equations (5) or (6), two boundary conditions must be provided. The first represents the behaviour of the flow far ahead and behind the blade, and the second represents the flow tangency condition (vanishing normal velocity) on the blade surface. In the inverse procedure presented here, the pressure distribution is used as an input rather than the blade physical co-ordinates, and our goal is to find the shape that the blade must have to achieve this input pressure distribution. Accordingly, for the inverse problem, neither a Neumann boundary condition for $\phi$ nor a Dirichlet boundary condition for $\psi$ can be given on the blade surface since its location is unknown *a priori*. This is in contrast to direct analysis methods where the blade geometry is known prior to the computational procedure. The problem of a prescribed pressure on a given blade configuration is ill-posed.[21] Here we prescribe a general pressure distribution and find the blade geometry that has a pressure distribution very close to this target pressure distribution.

## THE HODOGRAPH TRANSFORMATION

For two-dimensional irrotational flow, the non-linear equations (5) and (6) for steady flow can be rendered linear by changing the role of the dependent and independent variables. We introduce the complex velocity

$$u - \mathrm{i}v = q\mathrm{e}^{-\mathrm{i}\theta} \tag{7}$$

with $u, v, q$ and $\theta$ being functions of a complex variable

$$z = x + \mathrm{i}y. \tag{8}$$

Equations (4), (7) and (8) are then combined to yield the following total differential relation, viz.,

$$\mathrm{d}\phi + \mathrm{i}\frac{1}{\rho}\mathrm{d}\psi = q\mathrm{e}^{-\mathrm{i}\theta}\,\mathrm{d}z \tag{9}$$

From equation (9) with $q$ and $\theta$ as independent variables, and since $\rho = \rho(|\nabla\phi|)$, we find

$$\begin{aligned}\left(\frac{\partial z}{\partial\theta}\right)_q &= \frac{\mathrm{e}^{\mathrm{i}\theta}}{q}\left(\frac{\partial\phi}{\partial\theta} + \mathrm{i}\frac{1}{\rho}\frac{\partial\psi}{\partial\theta}\right),\\ \left(\frac{\partial z}{\partial q}\right)_\theta &= \frac{\mathrm{e}^{\mathrm{i}\theta}}{q}\left(\frac{\partial\phi}{\partial q} + \mathrm{i}\frac{1}{\rho}\frac{\partial\psi}{\partial q}\right).\end{aligned} \tag{10}$$

Differentiating the first of equations (10) with respect to $\theta$ and the second with respect to $q$ and then equating real and imaginary parts, we obtain the hodograph ($q$–$\theta$) equations, viz.,

$$\begin{aligned}\frac{\partial\phi}{\partial\theta} &= \frac{q}{\rho}\frac{\partial\psi}{\partial q},\\ \frac{\partial\phi}{\partial q} &= -\frac{1}{\rho q}(1 - M^2)\frac{\partial\psi}{\partial\theta}.\end{aligned} \tag{11}$$

In the present design procedure, it is essential to introduce the Prandtl–Meyer function $\nu$, defined by

$$\begin{aligned} \nu &= \int_{q^*}^{q} \sqrt{|1-M^2|}\frac{\mathrm{d}q}{q} \\ &= \int_{M=1}^{M} \frac{\sqrt{|1-M^2|}}{(1+\frac{\gamma-1}{2}M^2)}\frac{\mathrm{d}M}{M} \end{aligned} \tag{12}$$

in place of the velocity $q$ in equations (11), which then take their canonical form and become

$$\begin{aligned} \phi_\theta &= K(\nu)\psi_\nu, \\ \phi_\nu &= \pm K(\nu)\psi_\theta. \end{aligned} \tag{13}$$

Here the $\pm$ signs refer to supersonic and subsonic conditions respectively and

$$K(\nu) = K[\nu(M)] = [|1-M^2|]^{1/2}/\rho[q(M)].$$

A typical physical and hodograph plane representation (with $\nu$ and $\theta$ as hodograph variables) of the flow field is sketched in Figure 1 and 2. The blade maps into a closed curve containing the stagnation point $S$ at infinity and the sonic line at points $a, b$. The upstream and downstream singularities of the flow map into points $I_1$ and $I_2$ respectively. The analytical structure of $\psi$ near $\nu = 0$ and a smooth curvature of the blade at the sonic line require the local structure of the blade contour near the $\theta$-axis as sketched in Figure 3. This weakly singular behaviour (obtained from a limiting study of equations (13) as $\nu \to 0$) is of importance in the solution of the boundary-value problem, with $\psi$ given along the elliptic boundary (shaded line in detail of Figure 3). The region of the flow in Figure 1, bounded by the dotted contour and the blade, represents a region in

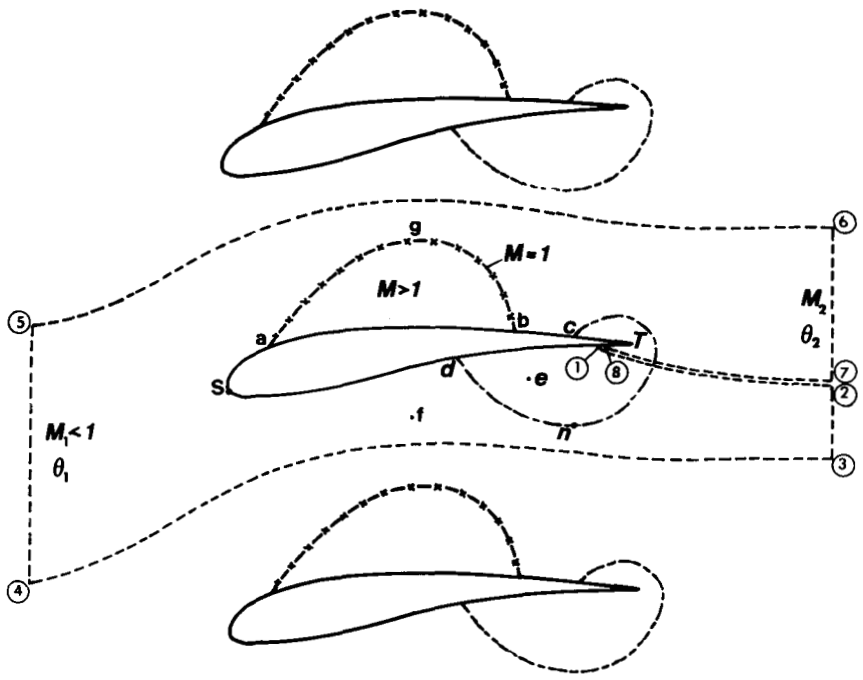


Figure 1. Sketch of shock-free flow past a rectilinear cascade; the dotted boundary 1–2–3–4–.... etc. represents the physical domain of interest

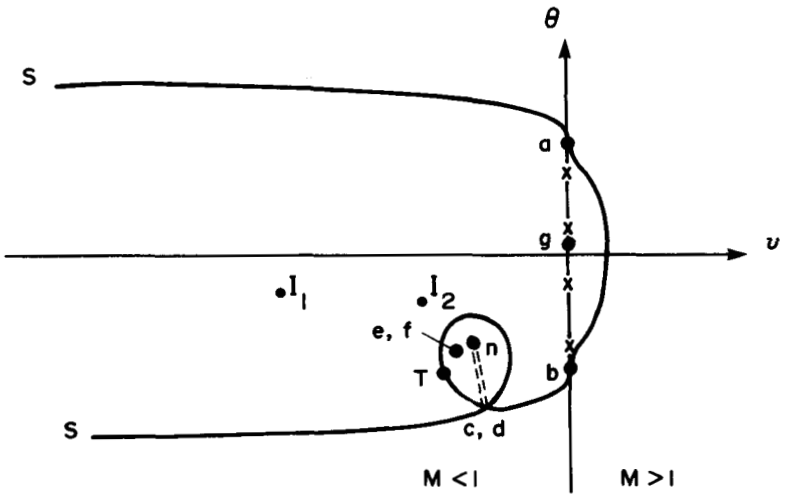


Figure 2. Hodograph plane representation of a single blade in a rectilinear cascade

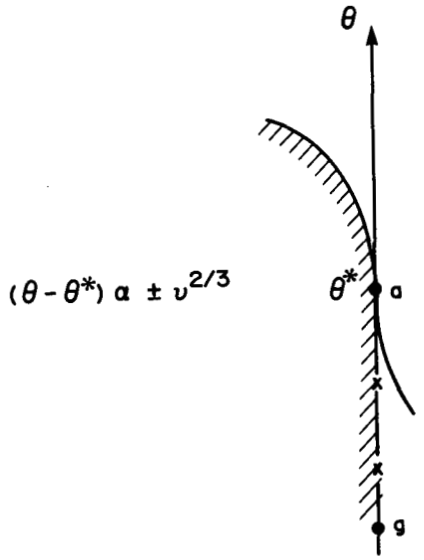


Figure 3. Asymptotic behaviour near points *a* or *b* on the sonic line in the hodograph plane

which every point has a velocity and flow angle equal to that of some other point outside this region, e.g. $q_e = q_f$ and $\theta_e = \theta_f$. Therefore, points *e* and *f* will correspond to the same point in the hodograph plane, which must be considered as a Riemann surface consisting of two sheets with a branch cut (lines *dn*, *cn*) connecting them. The local nature of this flow was studied by Lighthill[22] in his hodograph study of compressible flows past lifting aerofoils.

Since equations (13) are linear in the $v$–$\theta$ hodograph plane, there is usually no particular difficulty in finding solutions to them, by numerical methods if necessary. However, the presence of the second sheet of the two-sheeted Riemann surface and the *a priori* unknown location of the blade surface represent major obstacles in solving the governing equations in this plane. From

equations (13) it can also be shown that the second-order derivatives for both $\phi$ and $\psi$ form the Laplacian or the wave operator, depending on whether or not the flow is subsonic or supersonic. Thus the equations for the subsonic portion of the flow are invariant in their general form under a conformal transformation.

## DECOUPLING OF THE SUBSONIC FLOW DOMAIN

We proceed by assuming a conformal map of the subsonic portion of the two-sheeted Riemann surface of Figure 2 into the unit circle of Figure 4. (The double-connected infinite domain is mapped into a finite simply connected domain through an exponential mapping which is then followed by a square root mapping to unfold the Riemann sheets.) Here, part of the circumference of the unit circle corresponds to the blade surface which is wetted by subsonic flow; the remaining part corresponds to the sonic line. The segment comprising the sonic line, $\omega_a \leqslant \omega \leqslant \omega_b$, is chosen and the Mach number $M$ (or equivalently the pressure) on the subsonic part of the blade is prescribed. On the sonic line segment the Mach number is equal to one. Because Bernoulli's equation provides a correspondence between the values of $p$ and the local sound speed, we may formulate the inverse-design problem in terms of either $M$ or $p$, and our choice of $M$ is only a matter of convenience. A typical choice of $M$ for a supercritical blade with a cusped trailing edge is illustrated in Figure 5.

With the Mach number given on the boundary of the unit circle, and with the subsonic portion of the flow inside the circle, we take advantage of the fact that the mapping to the $\xi_0$-plane is conformal. Thus, the Prandtl–Meyer function $\nu$ and the flow deflection angle $\theta$ are conjugate harmonics, i.e.,

$$F(\xi_0) = \nu + \mathrm{i}\theta$$

or

$$\nabla^2 \nu(\xi_0) = 0, \tag{14}$$

$$\nabla^2 \theta(\xi_0) = 0. \tag{15}$$

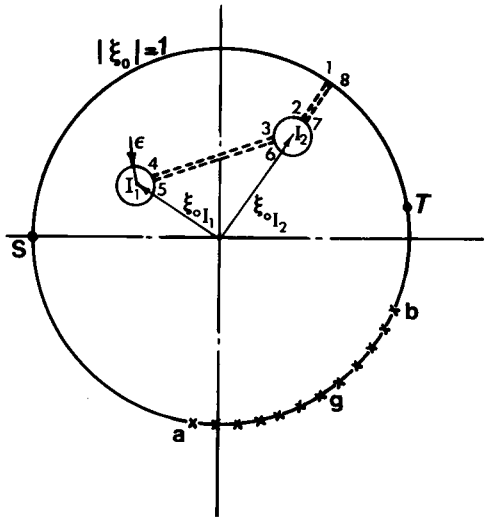


Figure 4. Cascade subsonic–sonic boundary in the $\xi_0$ plane (stagnation point $S$, trailing edge $T$, upstream singularity $I_1$, downstream singularity $I_2$)

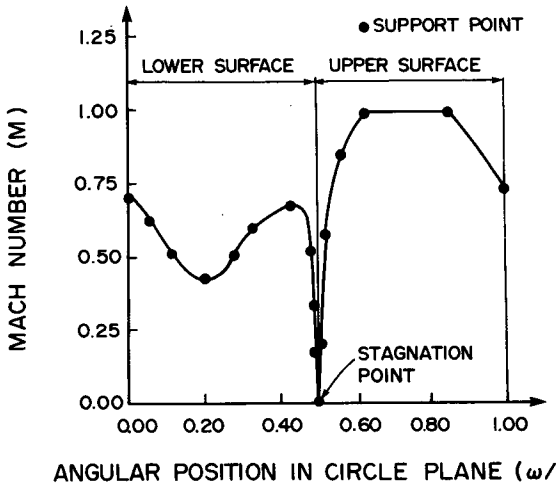


Figure 5. Typical input subsonic–sonic Mach number distribution

Here, $F(\xi_0)$ is the mapping function and $\xi_0 = re^{i\omega}$, with $r$ and $\omega$ being the radial and angular co-ordinates measured in the $\xi_0$-plane. Boundary conditions for equation (14) are provided through the use of equation (12) relating $\nu$ and $M$; that is, knowing the Mach number distribution on the unit circle, we calculate $\nu$ employing equation (12). We then solve Laplace's equation for $\nu$ inside the unit circle using Fourier series, which accordingly determines the flow deflection angle $\theta$ to within an arbitrary constant. However, the Prandtl–Meyer function $\nu$ is logarithmically singular in $q$ ($\nu \propto \log(q)$) at the stagnation point $S$, which for convenience is positioned at $\xi_0 = -1$ in the $\xi_0$-plane. Therefore, in order to solve the boundary value problem for $\nu$ using Fourier series we need first to subtract the logarithmic behaviour at point $S$. This is done as follows:

let

$$\bar{F}(\xi_0) = F(\xi_0) - \log(\xi_0 + 1),$$

$$G(\xi_0) = \nu(\xi_0) - \mathrm{Re}\{\log(\xi_0 + 1)\},$$

$$H(\xi_0) = \theta(\xi_0) - \mathrm{Im}\{\log(\xi_0 + 1)\},$$

then equations (14) and (15) become

$$\nabla^2 G(\xi_0) = 0 \tag{16}$$

$$\nabla^2 H(\xi_0) = 0 \tag{17}$$

Here $\mathrm{Re}\{\cdots\}$ and $\mathrm{Im}\{\cdots\}$ are the real and imaginary parts of $\log(\xi_0 + 1)$ respectively. Equation (16) is then solved inside the unit circle using a discrete Fourier series subject to the following boundary condition,

$$G(r = 1, \omega) = \nu(1, \omega) - \mathrm{Re}\{\log(e^{i\omega} + 1)\}.$$

Having obtained the solution for $G(r, \omega)$ in the unit circle, we then add back the logarithmic singularity to preserve the singular behaviour of $\nu$ at the stagnation point $S$.

Reformulating the definitions for the partial derivatives in equations (13) in terms of $r$ and $\omega$ we obtain

$$\phi_r = -\frac{1}{r} K(\nu)\psi_\omega,$$

and (18)

$$\phi_\omega = rK(\nu)\psi_r.$$

Eliminating $\phi$ through cross-differentiation of equation (18), we find the governing equation for the stream function $\psi$, viz.,

$$r^2\psi_{rr} + r\psi_r + \psi_{\omega\omega} = f(M)\{r^2 v_r \psi_r + v_\omega \psi_\omega\}. \tag{19}$$

Here, $K$ is a function of $M$, $M$ is a function of $v$ through equation (12), and

$$f(M) = -\frac{\gamma+1}{2} M^4 (1-M^2)^{-3/2}. \tag{20}$$

In the present formulation, equation (19) is the $\xi_0$-plane counterpart of the physical-plane equation (5) for the stream function. The transformation to hodograph variables $v$, $\theta$, followed by a conformal transformation to the $\xi_0$-plane, results in a linear second-order partial differential equation (Poisson Equation) for $\psi$. In addition to this linearity, the major advantages of these two transformations are the unfolding of the two-sheeted hodograph surface to a single sheet, and the representation of the subsonic–sonic boundary of the unknown blade by a unit circle. However, these advances are not without attendant complexities, albeit minor ones. These difficulties include the singularity in $f(M)$ in equation (20) at $M = 1$, and the presence of points $I_1, I_2$ which represent the upstream and downstream singularities of the flow inside the unit circle depicted in Figure 4. The first of these difficulties is circumvented by assuming that the Mach number on the sonic line is slightly less than 1, e.g. $M_{\text{sonic}} = 0{\cdot}995$, and using the local asymptotic behaviour of $\psi$ to extend the results to $M = 1$. That is, in a limiting process as $M \to 1$ we conclude from the asymptotic forms of equations (12) and (19) that $\psi_r \propto v^{-1/3}$ along the sonic line. The second of these difficulties is circumvented through a numerical co-ordinate transformation of the $\xi_0$-plane into the rectangular computational $(s,t)$ plane shown in Figure 6. To exclude the two singularities at points $I_1, I_2$ from the $\xi_0$-plane, referring to Figure 4, we introduce two branch cuts; the first 3–4–5–6 connecting the two circles with radii $\varepsilon$ and centres at points $I_1$, $I_2$, and the second connecting the circle with centre at $I_2$ and any point on the subsonic blade surface (i.e. on the unit circle). To maintain consistency with the physical boundary conditions, periodic numerical boundary conditions are imposed along the branch cut 1–2, 7–8. It is noteworthy to mention here that in a direct procedure where the blade shape is prescribed, the second branch cut would be equivalent to an initial guess made for the wake position. Conversely, in the present formulation, since the blade shape is unknown *a priori*, a branch cut connecting any point on the subsonic surface of the blade (not necessarily the trailing edge)

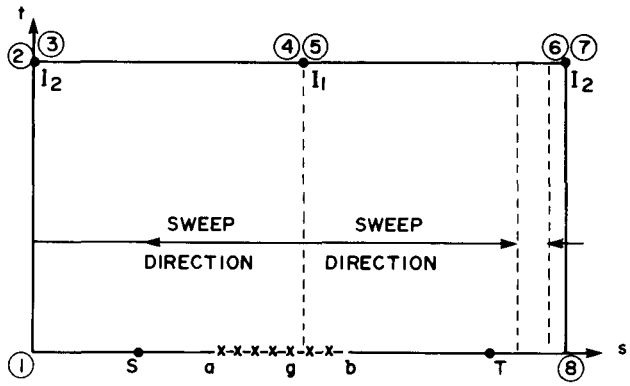


Figure 6. Computational plane image of the $\xi_0$ plane as $\varepsilon \to 0$. Periodic boundary conditions are imposed on 1–2, 7–8. The dotted lines represent grid lines. The location of the trailing edge $T$ is not known in advance but is found as part of the solution

to the outflow boundary is used; see Figure 1. The resulting simply connected domain $S$–1–2–3–4–5–6–7–8–$b$–$a$–$S$ is then numerically mapped to the rectangular computational $s$–$t$ plane ($0 \leqslant s \leqslant 2\pi, 0 \leqslant t \leqslant 1$) depicted in Figure 6. The non-orthogonal boundary-fitted grid is generated using the Thompson, Thames, Mastin (TTM) method[23] which employs the following inhomogeneous Laplace equations as the generating system,

$$\begin{aligned} s_{\bar{x}\bar{x}} + s_{\bar{y}\bar{y}} &= P(s,t), \\ t_{\bar{x}\bar{x}} + t_{\bar{y}\bar{y}} &= Q(s,t). \end{aligned} \tag{21}$$

Here, $\bar{x} = r\cos(\omega)$, $\bar{y} = r\sin(\omega)$, and $P, Q$ are arbitrary functions which provide means for controlling the resolution of the resulting mesh system. With $s$ and $t$ as new independent variables, we obtain the following governing equation for $\psi(s,t)$, viz.,

$$\psi_{ss} + a(s,t)\psi_{tt} = b(s,t)\psi_s + c(s,t)\psi_t + d(s,t)\psi_{st}. \tag{22}$$

In equation (22), $a(s,t)$ and $d(s,t)$ are purely functions of the local Jacobian, $J = \partial(s,t)/\partial(\bar{x},\bar{y})$, and metrics of the transformation. The functions $b(s,t)$ and $c(s,t)$ are also functions of the local Jacobian, metrics of the transformation as well as the local Mach number $M$.

## NUMERICAL BOUNDARY CONDITIONS

On the blade surface wetted by subsonic flow we have

$$\psi(s,0) = 0 \quad s_b \geqslant s \geqslant s_c.$$

On the remaining portion of the lower boundary, i.e. the sonic line, an arbitrary distribution for the stream function $\psi$ is prescribed, viz.,

$$\psi(s,0) = \psi_{\text{sonic}} = g(s) \quad s_b \leqslant s \leqslant s_a.$$

The compressible upstream and downstream stream function distributions $\psi_{I_1}, \psi_{I_2}$ are related to their incompressible counterparts $\Psi_{I_1}, \Psi_{I_2}$ by the following relations,

$$\begin{aligned} \psi_{I_1} &= \frac{1}{k(v(M_1))}\Psi_{I_1} \\ &= \frac{1}{k(v(M_1))}\operatorname{Im}\{(1 + iA_1)\ln(\xi_0 - \xi_{0_{I_1}})\}, \\ \psi_{I_2} &= \frac{1}{k(v(M_2))}\Psi_{I_2} \\ &= \frac{1}{k(v(M_2))}\operatorname{Im}\{(A_2 + iA_3)\ln(\xi_0 - \xi_{0_{I_2}})\}. \end{aligned} \tag{23}$$

Here,

$$\begin{aligned} A_1 &= -\tan(\theta_1)/\sqrt{1 - M_1^2} \\ A_2 &= -\sigma\frac{M_2\cos(\theta_2)}{M_1\cos(\theta_1)}\sqrt{\frac{(1 - M_2^2)}{(1 - M_1^2)}}\sqrt{\frac{1 + \dfrac{\gamma - 1}{\gamma + 1}(M_1^2 - 1)}{1 + \dfrac{\gamma - 1}{\gamma + 1}(M_2^2 - 1)}}, \\ A_3 &= -\tan(\theta_2)/\sqrt{1 - M_2^2}. \end{aligned} \tag{24}$$

and

In equations (24), $M_1$ and $M_2$ are the upstream and downstream Mach numbers respectively, $\theta_1$, $\theta_2$ are the upstream and downstream flow deflection angles and $\sigma$ is the solidity of the cascade (i.e. gap-to-chord ratio). It is noteworthy to mention that equations (23) are a consequence of the fact that, at points $I_1$, $I_2$ which represent the upstream and downstream singularities in the $\xi_0$-plane, equations (18) reduce to the familiar Cauchy–Riemann equations (or incompressible flow equations) expressed in polar co-ordinates. Thus the complex potentials defining the upstream and downstream stream function distributions are those for an incompressible flow $\Psi_{I_1}$ or $\Psi_{I_2}$ which is related to its compressible counterpart $\psi_{I_1}$ or $\psi_{I_2}$ through equations (23). Equations (23) in conjunction with the solution to equations (21) are then employed to express the upstream and downstream stream function distributions in the $s$–$t$ plane, Figure 6. The condition of periodicity is imposed on the computational plane image of the branch cut 1–2, 7–8 shown in Figure 4. Continuity of the stream function $\psi$ across the branch cuts 3–4, 5–6 requires that $\psi(s,1) = \psi(2\pi - s, 1)$. This condition is satisfied by updating each $\psi$ value on the $t = 1$ line as soon as its corresponding value is altered by the line relaxation calculation. At points $I_1$, $I_2$ the stream function is singular. To remove this singular behaviour we let

$$\psi = \psi_1 + \psi_2 \tag{24a}$$

where $\psi_1$ is the singular portion due to sources and vortices at point $I_1$, $I_2$, and $\psi_2$ is a regular (non-singular) stream function. In the present formulation, $\psi_1$ is obtained through the use of equations (23), i.e.

$$\psi_1 = \mathrm{Im}\{\psi_{I_1} + \psi_{I_2}\}$$

where $\mathrm{Im}\{\ldots\}$ is the imaginary part of $\psi_{I_1}$, $\psi_{I_2}$. The Jacobian of the numerical mapping $J$ is also singular at points $I_1$, $I_2$ in the $s$–$t$ plane. To remove this singular behaviour of $J$ we define a new Jacobian $\bar{J}$ such that

$$\bar{J} = J\sqrt{\cosh(1-t) - \cos(2s)} \tag{24b}$$

Upon substitution of equations (24a) and (24b) into equation (22) we obtain a regularized two-dimensional stream function equation in terms of $\psi_2$, $\bar{J}$ and the derivatives of $\psi_1$ which are easily found from equations (23). Since the stream function is undefined to within a constant we set $\psi_{2_{I_1}}(\pi, 1) = 0$. To avoid special handling of the regularized stream function at $I_2$, we construct a grid system which excludes this point as a node.[3] At this juncture, it is important to emphasize that the physical plane image of the branch cut 3–4–5–6 does not represent two streamlines of the resulting flow; instead, two boundaries along which there is a variation in the stream function values are obtained.

The boundary value problem for $\psi_2$ is now complete, and equation (22), now expressed in terms of $\psi_2$, is solved iteratively using a second-order accurate line relaxation procedure. The sweep direction is indicated by the arrows in Figure 6. The stagnation streamline leaves the contour of the blade at a cusped or wedged trailing edge. This defines, in direct analysis, the amount of circulation around the blade and the location of the stagnation point near the leading edge. For an indirect method such as the present one, the situation is exactly the reverse: since the (mapped) stagnation point location is given, we have to vary either $M_2$ or $\theta_2$ for a fixed $M_1$, $\theta_1$ and solidity $\sigma$. In the present formulation, $M_2$ is fixed and $\theta_2$ is initially guessed and then left free. Hence its correct value is determined as part of the solution. The mapped location $T$ of the trailing edge results from this adjustment and the trailing edge shape is then cusped. In the computational plane the stagnation streamline leaves the blade contour at point $T$ at a 90° angle.

The results for the gradients $\psi_s(s,0)$ and $\psi_t(s,0)$ along the elliptic boundary consisting of the

subsonic portion of the blade and the sonic line are then used in finding the inverse-map to the physical plane, equation (9), which can be written as

$$\begin{aligned} \mathrm{d}x(s,0) &= \frac{1}{q}\{K(v)\cos(\theta)\psi_t(s,0) - \frac{1}{\rho}\sin(\theta)\psi_s(s,0)\}\,\mathrm{d}s, \\ \text{and} \\ \mathrm{d}y(s,0) &= \frac{1}{q}\{K(v)\sin(\theta)\psi_t(s,0) + \frac{1}{\rho}\cos(\theta)\psi_t(s,0)\}\,\mathrm{d}s. \end{aligned} \tag{25}$$

Equation (25) are then numerically integrated along the subsonic–sonic boundary of the computational plane ($t = 0, 0 \leqslant s \leqslant 2\pi$) starting from the trailing edge $T$ on the blade's lower surface moving toward the stagnation point $s$, sonic points $a, b$, and finally ending at the trailing edge $T$ on the blade's upper surface, i.e.,

$$\begin{aligned} x &= x_0 + \int_{s_T}^{s} \mathrm{d}x(s), \\ y &= y_0 + \int_{s_T}^{s} \mathrm{d}y(s), \end{aligned} \qquad 0 \leqslant s \leqslant 2\pi. \tag{26}$$

The resulting subsonic–sonic line configuration is then checked to see if it has a reasonable thickness distribution (i.e. reasonable trailing edge gaps and no contour crossings). If not, then the input design parameters must be altered and the design procedure repeated. When a suitable subsonic–sonic line configuration is found, the first of equations (18) is numerically integrated to find the potential distribution along the elliptic boundary, i.e.,

$$\phi(1,\omega) = \phi_0(1,\omega) - \int_0^{2\pi} K(v)\psi_\omega(1,\omega)\,\mathrm{d}r. \tag{27}$$

Results obtained from the solution of the subsonic flow region on the sonic line (i.e. $\phi_{\text{sonic}}$, $x_{\text{sonic}}$, $y_{\text{sonic}}$) are then used in addition to the prescribed sonic line stream function $\psi_{\text{sonic}}$ as initial values for solving the supersonic flow (considering the + sign in equations (13)) in the hodograph plane using the method of characteristics described below.

## SUPERSONIC FLOW DOMAIN

It follows from equations (13) for the flow in the embedded supersonic region that both $\psi$ and $\phi$ satisfy the linear wave equations

$$\psi_{vv} - \psi_{\theta\theta} = -\frac{1}{K(v)}\left[\frac{\partial}{\partial v}K(v)\right]\psi_v, \tag{28}$$

and

$$\phi_{vv} - \phi_{\theta\theta} = -K(v)\left[\frac{\partial}{\partial v}\frac{1}{K(v)}\right]\phi_v. \tag{29}$$

The above equations have two real characteristics whose slopes are given by

$$\frac{\mathrm{d}v}{\mathrm{d}\theta} = \pm 1. \tag{30}$$

Introducing the characteristic co-ordinates $\xi, \eta$ defined by

$$\begin{aligned} \xi &= v + \theta, \\ \eta &= v - \theta, \end{aligned} \tag{31}$$

and reformulating the partial derivatives in equations (13) in terms of the new co-ordinates, we obtain

$$\phi_\xi = K(\nu)\psi_\xi, \qquad \phi_\eta = -K(\nu)\psi_\eta. \tag{32}$$

and

Equations (32) may also be expressed in total differential form as
on $\xi = \text{constant}$

$$\mathrm{d}\phi + K(\nu)\,\mathrm{d}\psi = 0, \qquad \mathrm{d}\phi - K(\nu)\,\mathrm{d}\psi = 0. \tag{33}$$

and on $\eta = \text{constant}$

With the stream function $\psi_{\text{sonic}}(\theta)$ and the potential $\phi_{\text{sonic}}(\theta)$ data known on the sonic like with co-ordinates $x_{\text{sonic}}(\theta)$ and $y_{\text{sonic}}(\theta)$, we proceed to solve equations (33), which hold along the two families of characteristics, using a step-by-step numerical scheme. The basic concept of this scheme is the following:

Through each point A, B, C, D, E, F of the sonic line (line AF in Figure 7 two Mach lines pass, one of the first family, $\eta = \text{constant}$ $(a_1, b_1, c_1, \ldots, f_1)$, and one of the second family, $\xi = \text{constant}$ $(a_2, b_2, c_2, \ldots, f_2)$. Since the flow properties at the points of the line AF are known, the constants of equations (33) for each characteristic line $a_1 \ldots f_1, a_2, \ldots f_2$, at each point of AF, are also known. Consequently, equations (33) applied along two characteristics of opposite families, e.g. $b_1$ and $a_2$ of Figure 7, give two equations relating $\phi_G$ to $\psi_G$. These can be solved to obtain $\phi$ and $\psi$ at point G as functions of $\phi$ and $\psi$ at the points A and B, viz.,

$$\psi_G = \frac{1}{2}(\psi_A + \psi_B) + \frac{1}{2K(\nu)}(\phi_A - \phi_B),$$
$$\phi_G = \frac{1}{2}(\phi_A + \phi_B) + \frac{K(\nu)}{2}(\psi_A - \psi_B). \tag{34}$$

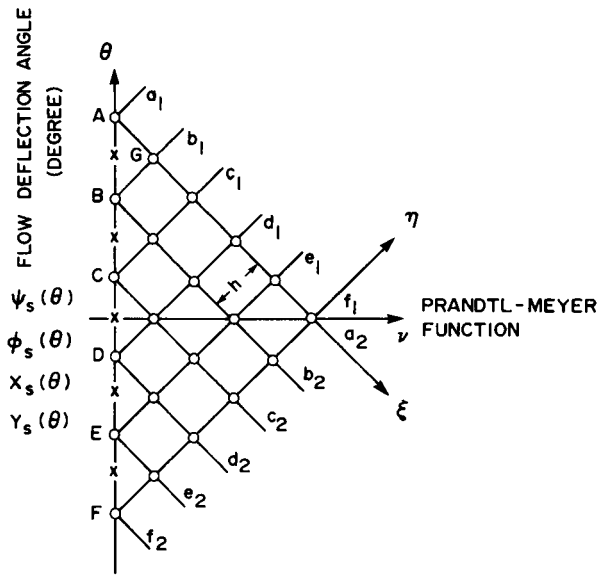


Figure 7. Computation of the supersonic flow field in the hodograph plane using the method of characteristics

In equations (34), if we think of $\nu$ as a specified function of $\xi$ and $\eta$ on a rectangular grid, the coefficient $K(\nu)$ may be approximated by average values such that the numerical step-by-step scheme becomes second-order accurate in the mesh size, $h$. The flow deflection angle $\theta$, and the prandtl–Meyer function $\nu$, are evaluated at the grid nodes using equations (31).

Having solved for the flow properties at all grid nodes, we then proceed to search for points of zero streamline values as they represent points on the blade's upper surface.

The inverse transformation from the hodograph $\nu$–$\theta$ plane to the physical $x$–$y$ plane is given by equation (9), which could be written at every grid point as

$$\begin{aligned} \mathrm{d}x &= \frac{\cos(\theta)}{q}\mathrm{d}\phi - \frac{\sin(\theta)}{\rho q}\mathrm{d}\psi, \\ \mathrm{d}y &= \frac{\sin(\theta)}{q}\mathrm{d}\theta + \frac{\cos(\theta)}{\rho q}\mathrm{d}\psi. \end{aligned} \tag{35}$$

The Jacobian of the transformation is

$$\begin{aligned} J &= \frac{\partial(x,y)}{\partial(\nu,\theta)} = \frac{\partial(\phi,\psi)}{\partial(\nu,\theta)}\left[\frac{\partial(\phi,\psi)}{\partial(x,y)}\right]^{-1} \\ &= \frac{1}{\rho q^2}(\phi_\nu\psi_\theta - \phi_\theta\psi_\nu). \end{aligned} \tag{36}$$

Using equations (13) to eliminate $\phi_\nu$ and $\phi_\theta$ in terms of $\psi_\nu, \psi_\theta$, we find that for supersonic flow

$$J = \frac{K(\nu)}{\rho q^2}(\psi_\theta^2 - \psi_\nu^2) \tag{37}$$

which indicates the possibility of a vanishing Jacobian whenever $|\psi_\theta| = |\psi_\nu|$. It can be easily shown from equations (32) that this condition is satisfied whenever a $\psi$ = constant line is tangent to the characteristics in the hodograph $\nu$–$\theta$ plane, i.e. whenever $\psi_\eta = 0$ or $\psi_\xi = 0$. The locus of points in the hodograph plane for which $J = 0$ is known as a limit line. In the physical plane the image of such a line is a cusped curve along which the physical surface can be thought to be folded upon itself.[24] Such limit lines indicate the inconsistency of the sonic line data with shock-free flow. Thus, they are only acceptable if they occur below the blade's upper surface. However, if they occur above or on the blade's upper surface, the sonic line data must be altered by adjusting the input subcritical pressure or the sonic line stream function distribution or both, and the design procedure repeated.

## COMPUTER PROGRAM PACKAGE

The computer program package consists of eighteen FORTRAN IV subroutines performing calculations and data transfer. The package makes use of two permanent files for results to be retained and one file for input data. For a specific blade design, the program has to be operated in the following manner:

1. Using the input Mach numbers $M_1$, $M_2$, flow deflection angle $\theta_1$, subsonic–sonic Mach number distribution, sonic line stream function distribution $\psi_{\text{sonic}}$, and an initial guess for $\theta_2$, we obtain a subsonic–sonic boundary configuration which is stored on one of the permanent files accessible to the code.
2. To reduce the $x$-gap at the trailing edge of the resulting blade (which is usually open), we alter slightly the levels of the input Mach number distribution, say on the upper or lower surface of the blade. This in turn has the direct effect of changing locations of the singularities at $I_1$ and

$I_2$ in the $\xi_0$-plane which consequently result in the reduction of the $x$-gap to a preset value, e.g. $10^{-3}$.

3. To reduce the $y$-gap at the trailing edge of the resulting blade, we alter the slopes of the input Mach number in the vicinity of the stagnation point $S$. That is, steeper slopes usually result in a blade with a smaller leading edge radius and hence a smaller maximum thickness and eventually a smaller $y$-gap.
4. Once an acceptable (i.e. no contour crossings) subsonic–sonic boundary configuration is obtained, the supersonic flow field computation is then carried out to determine the blade coordinates under the sonic line. If a limit line is encountered in the supersonic flow domain, steps 1 to 3 above are repeated for a modified input sonic line stream function distribution.

## COMPUTATIONAL RESULTS AND DISCUSSION

It should be mentioned here that the primary objective of this research was to demonstrate through many numerical examples that the method accurately predicts the blade geometry which corresponds to an input target pressure. This objective, however, dictated that we compare our results with those obtained from a direct computation of the flow past the designed blade rather than with those obtained from an alternative design method. The analysis code used in this study is that of Reference 5 which is based on the numerical solution of the full potential equation expressed in conservative form.

Three examples illustrating the performance and application of the design procedure using an IBM 3081 computer are given in Figures 8, 9 and 10. Numerical computations were performed on a $200 \times 64$ mesh in the $s$–$t$ plane requiring a maximum CPU time of 2 minutes. The preset values for the $x$ and $y$ trailing edge gaps were $10^{-3}$ and $10^{-2}$ respectively. With a trailing edge gap, the resulting blade configuration lends itself to viscous boundary layer corrections when displacement effects are later incorporated.[25,26]

The first example is that of a shock-free compressor stator blade (solidity = 1·0) with a cusped trailing edge. The inflow Mach number $M_1$, outflow Mach number $M_2$, and flow deflection angle $\theta_1$ are 0·75, 0·652 and $-35°$ respectively. For this blade, the converged solution results in an outflow turning angle $\theta_2$ of 3·17°. For this example, Figure 8 illustrates the input subsonic–sonic Mach number distribution, the equivalent pressure ($C_p$) distribution, and the resulting blade geometry. A comparison with results obtained from the direct computation of the flow field, using the designed blade geometry as input, is also illustrated in Figure 8. The agreement between our results and those obtained from the direct computation of the flow is very good in the subsonic regions and fair in the supersonic region. The slight disagreement in the pressure distributions in the vicinity of the trailing edge is undoubtedly related to the size of the $y$-gap at this location. This discrepancy could be further reduced by reducing the $y$-gap tolerance (e.g. $10^{-3}$) which is preset in the inverse code. This, however, results in a larger number of inverse iterations (almost twice the number required for a gap tolerance of $10^{-2}$) and hence increases the CPU time.

Experience has shown that at least two modifications of the input Mach number distribution at the trailing edge are required to obtain a reasonable (i.e. no contour crossings) blade configuration. It is noteworthy to mention that the slightly different Mach number distributions do, of course, give two slightly different shock-free blade designs. That is, only one blade configuration is obtained for a given Mach number distribution. In our procedure, Volpe and Melnik's[21] first constraint on the existence of a solution to the inverse problem is implicitly satisfied since we do allow for slight variations in the prescribed input pressure distribution.

Figure 9 illustrates the input subsonic–sonic Mach number distribution for a compressor stator blade (solidity = 0·85) with a cusped trailing edge. The prescribed inflow conditions are $M_1 = 0·75$,

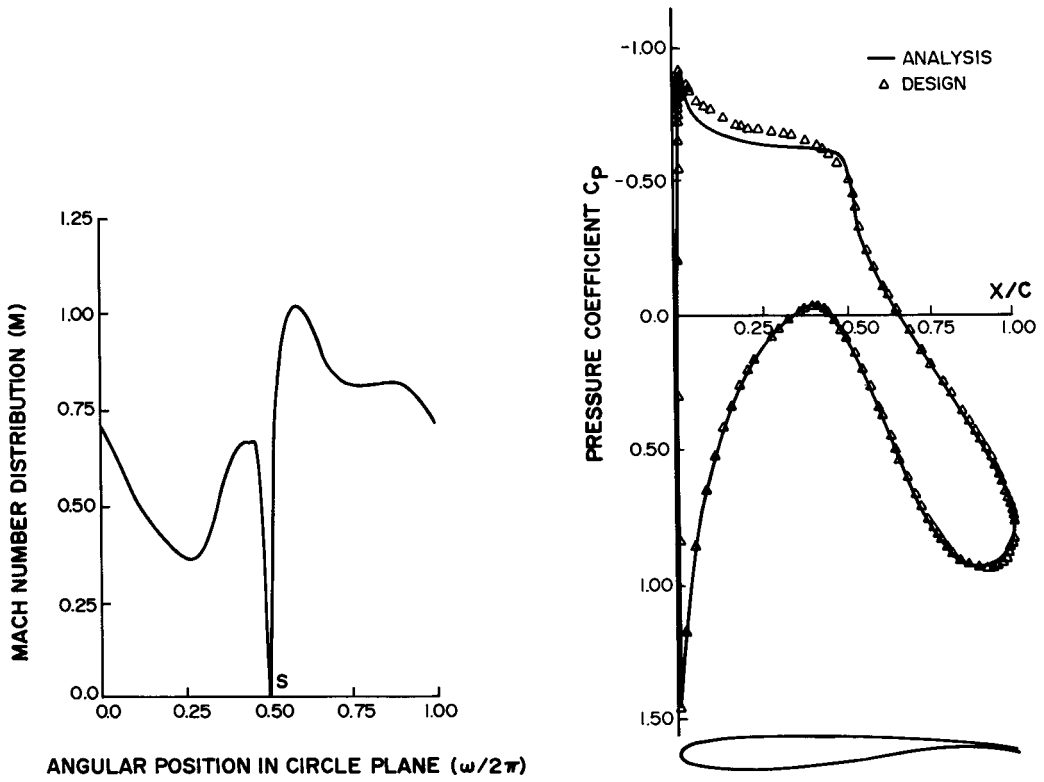


Figure 8. Shock-free compressor blade and its corresponding Mach number and pressure distributions ($M_1 = 0{\cdot}750$, $M_2 = 0{\cdot}652$, $\theta_1 = -35{\cdot}0°$, $\theta_2 = -3{\cdot}17°$, solidity = 1·0)

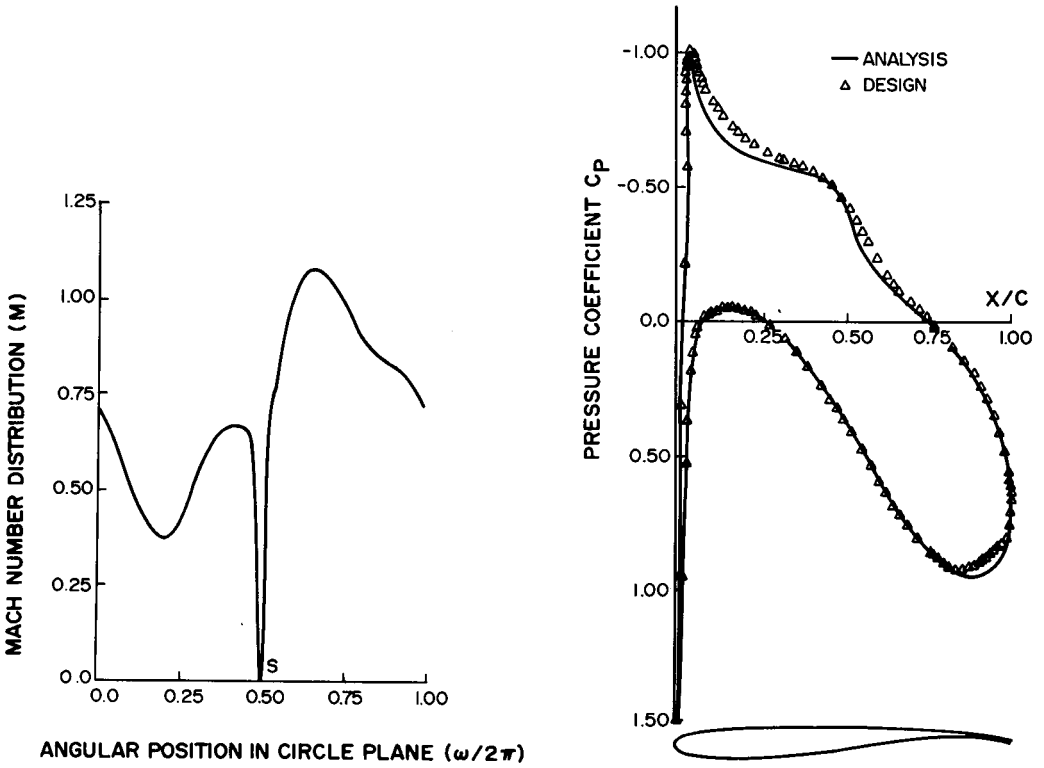


Figure 9. Shock-free compressor blade and its corresponding Mach number and pressure distributions ($M_1 = 0{\cdot}750$, $M_2 = 0{\cdot}600$, $\theta_1 = -30{\cdot}0°$, $\theta_2 = -7{\cdot}82°$, solidity = 0·85)

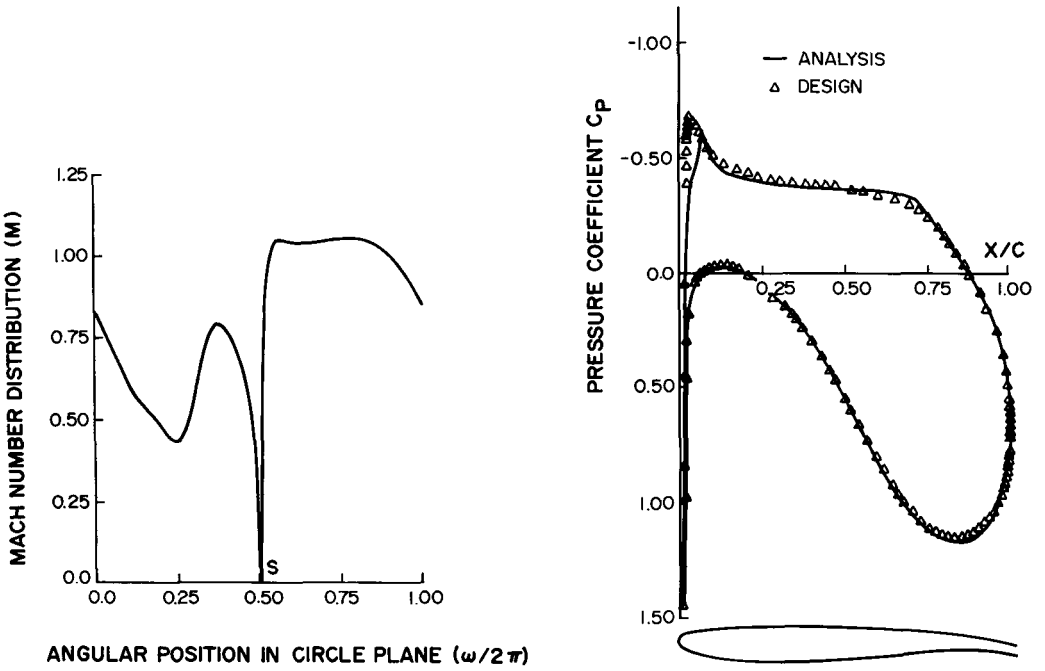


Figure 10. Shock-free compressor blade and its corresponding Mach number and pressure distributions ($M_1 = 0{\cdot}680$, $M_2 = 0{\cdot}570, \theta_1 = -40{\cdot}0°, \theta_2 = -5{\cdot}624°$, solidity $= 0{\cdot}792$)

and $\theta_1 = -30°$. The converged inverse solution results in an outflow turning angle $\theta_2 = -7{\cdot}82°$ if the outflow Mach number is set at $M_2 = 0{\cdot}60$. The resulting blade geometry and a comparison with the results obtained from the direct computation of the flow past the designed blade are also shown in Figure 9. Again, the slight disagreement which is noticed between the $C_p$ distributions in the trailing edge region is attributed to the size of the existing $y$-gap at the trailing edge of the designed blade.

The final example represents the design of a compressor stator blade (solidity $= 0{\cdot}791$) with a cusped trailing edge. The prescribed design conditions are: at inflow $M_1 = 0{\cdot}68$, $\theta_1 = -40{\cdot}0°$, at outflow $M_2 = 0{\cdot}57$. The flow deflection angle at outflow $\theta_2$ was found to be $-5{\cdot}62°$ as part of the numerical solution. For this example, Figure 10 illustrates the input subsonic–sonic Mach number distribution, the equivalent pressure ($C_p$) distribution, and the resulting blade geometry. A comparison of the $C_p$ distribution with that obtained from the direct computation of the flow past the designed blade is also given in Figure 10.

## CONCLUDING REMARKS

An inverse procedure has been developed for the global design of shock-free compressor cascades. The procedure is as simple as possible from a user's point of view and merely requires as input a pressure distribution, a sonic line stream function distribution, in addition to three of the design conditions representing the inflow and outflow. Although the method has some limitations, most notably in its application to choked flows, it is expected to yield good designs in many practical cases. Moreover, although the results are given for inviscid flow, the same procedure can be employed iteratively with a boundary-layer calculation (using blade profiles with an open trailing edge) in order to achieve viscous blade designs. Although this paper concentrates on the design of

compressor blades, the procedure is quite general and is currently being used in the design of shock-free turbine blades.

## REFERENCES


1. A. Shapiro, *The Dynamics and Thermodynamics of Compressible Fluid Flow*, The Ronald Press Company, New York, 1954.
2. H. W. Liepmann and A. Roshko, *Elements of Gas Dynamics*, Wiley, New York, 1957.
3. D. C. Ives and J. F. Liutermota, 'Analysis of transonic cascade flow using conformal mapping and relaxation techniques', *AIAA Paper No. 76-370*, July 1976.
4. J. R. Caspar, D. E. Hobbs and R. L. Davis, 'The calculation of potential flow in cascades using finite area techniques', *AIAA Paper No. 79-0077*, January 1979.
5. C. Farrel and J. Adamczyk, 'Full potential solution of transonic quasi-3-D flow through a cascade using artificial compressibility', *NASA TM81637*, March 1981.
6. J. D. Denton, 'A time marching method for two- and three-dimensional blade to blade flows', Aeronautical Research Council, R&M No. 3775, London, October 1974.
7. P. R. Garabedian, *Partial Differential Equations*, Wiley, New York, 1964.
8. E. V. Swenson, 'Geometry of the complex characteristics in transonic flow', *Communications on Pure and Applied Mathematics*, **XXI**, 175–185 (1968).
9. D. Korn, 'Numerical design of transonic cascades', Courant Institute of Mathematical Sciences, ERDA Research and Development Report C00-3077-72, January 1975.
10. H. Sobieczky, 'Entwurf uberkritischer profile mit hilfe der rheoelektrischen analogie', *DFVLR-FB 75-43*, 1975.
11. H. Sobieczky, 'Related analytical, analog and numerical methods in transonic airfoil design', *AIAA Paper No. 79-1556*, July 1979.
12. H. Sobieczky, 'Transonic fluid dynamics—lecture notes', The University of Arizona, TFD 77-01, October 1977.
13. D. S. Dulikravich and H. Sobieczky, 'CAS22-FORTRAN program for fast design and analysis of shock-free airfoil cascades using fictitious gas concept', *NASA CR 3507*, January 1982.
14. D. S. Dulikravich and H. Sobieczky, 'Design of shock-free compressor cascades including viscous boundary layer effects', *ASME Paper No. 83-GT-134*, October 1983.
15. P. P. Beauchamp, 'A numerical tool for the design of shock-free transonic cascades', *M. S. Thesis*, The University of Arizona, Tucson, Arizona, August 1981.
16. J. F. Carey and T. T. Pan, 'Shock-free redesign using finite elements', *Proc. Int. Conf. on Inverse Design Concepts*, Austin, Texas, pp. 283–295, October 1984.
17. D. S. Dulikravich and H. Sobieczky, 'Shockless design and analysis of transonic blade shapes', *AIAA Paper No. 81-1237*, June 1981.
18. N. J. Yu, 'An efficient transonic shock-free redesign procedure using a fictitious gas method', *AIAA Paper No. 79-0075*, June 1979.
19. A. A. Hassan, 'Subcritical and supercritical airfoils for given pressure distributions', *Ph.D. Dissertation*, The University of Arizona, Tuscon, Arizona, August 1981.
20. A. A. Hassan, H. Sobieczky and A. R. Seebass, 'Subsonic airfoils with a given pressure distribution', *AIAA Journal*, **22**, No. 9, 1185–1191 (1984).
21. G. Volpe and R. E. Melnik, 'The role of constraints in the inverse design problem for transonic airfoils', *AIAA Paper No. 81-1233*, June 1981.
22. M. J. Lighthill, 'On the hodograph transformation for high speed flow', *Quart. J. of Mech. and Appl. Math.*, **1**, 442–450 (1948).
23. J. F. Thompson, F. C. Thames and C. W. Mastin, 'Automatic numerical generation of body-fitted curvilinear coordinate systems for fields containing any number of arbitrary two-dimensional bodies', *J. Comp. Phys.*, **15**, 299–319 (1974).
24. A. R. Manwell, *The Hodograph Equations*, Oliver and Boyd, Edinburgh, 1971.
25. A. A. Hassan, 'The design of shock-free supercritical airfoils including viscous effects', *Commun. Appl. Numer. Methods* **2**, 37–45 (1986).
26. A. A. Hassan, 'A viscous–inviscid coupling method for the design of low Reynolds number airfoil sections', *Proc. Conf. Low Reynolds Number Airfoil Aerodynamics*, Notre Dame, Indiana, pp. 53–63, June 1985.